

Nanosheets Derived through Dissolution-Recrystallization of TiB₂ as Efficient Anode for Sodium-Ion Batteries

Shruti Suriyakumar,^[a] Akash Varma,^[b] Vishnu Surendran,^[a] Kabeer Jasuja,^{*[b]} and M. M. Shajumon^{*[a]}

Metal borides when subjected to dissolution and recrystallization exhibit a tendency to grow preferentially in lateral dimensions and form nanosheets. Such derived nanosheets exhibit unusual properties that can potentially be used in energy conversion and storage applications. Here we report boride-based nanosheets derived from titanium diboride through a scalable one-pot chemical approach as a sodium-ion battery anode material. The half-cell with TiB₂-derived nanosheets (TiB₂-NS) as anode delivers an initial discharge capacity of 252 mAh g⁻¹ at 0.1 A g⁻¹, and appreciable cycling stability is

achieved at 1 A g⁻¹ current density. Further, a sodium-ion full cell assembled with TiB₂-NS as anode and sodium vanadium phosphate/carbon as cathode is demonstrated. The full cell delivers an energy density of 111 Wh kg⁻¹ at a power density of 500 W kg⁻¹. Being the first report of its kind, our study exemplifies the rich potential that the TiB₂-NS deliver as an anode material upon nanoscaling and substantiates the theoretical prediction on using transition metal boride-based anode material for sodium-ion battery.

1. Introduction

In a world that is increasing its reliance on wind, solar, and hydroelectric power, low cost and efficient energy storage devices to store such intermittent energy is the need of the hour.^[1,2] The current lithium-ion battery (LIB) technology is reaching its limits in terms of cost and storage capacity. Owing to the increased abundance and energy density close to LIBs, sodium-ion batteries (SIBs) are promising alternatives for such grid storage applications.^[3] Among other post-lithium ion technologies, we can also envision SIBs as sustainable lower-cost alternatives to LIBs for applications such as short-range electric vehicles.^[4] Though LIBs and SIBs work based on the rocking chair mechanism, it is not possible to pick electrode materials for SIBs that are analogues to those used in LIBs and expect similar electrochemical performance.^[5–7] One such classic example is graphite which is widely used in LIBs as anode material and cannot be directly applied to SIBs due to the weak interaction between sodium and graphite.^[8] In this regard, finding materials for efficient sodium-ion storage is a challenging task.

Two-dimensional (2D) materials have gained considerable interests in the fields of electrochemical energy storage and

conversion systems due to their extraordinary properties. They can offer an ultra-high surface area for Na⁺ intercalation and provide a short distance for Na⁺ migration, making this class of materials rather attractive for SIBs.^[9] However, relatively few experimentally realized 2D structures could serve as anode materials for SIBs. Intercalation chemistry of alkali metal cation was first reported in transition metal dichalcogenides (TMDs) in 1970s.^[10] MoS₂, VS₂, TiS₂ and NiS₂, SnS and FeS₂ have been widely studied as 2D anode material.^[11–14] Mortazavi et al.^[15] reported that the layered MoS₂ could be used as the anode material for SIBs, which has a maximum theoretical capacity of 146 mAh g⁻¹. DFT calculations prove that the NiS₂ surface has a high chemical affinity towards Na ions, promising the concentration of Na ion on the surface for fast redox reactions during sodiation/de-sodiation of NiS₂. 2D materials such as MXene, Ti₂C,^[16] V₂C,^[17,18] and Nb₂C^[19] have exhibited desired properties as electrode materials for LIBs and SIBs. In this direction, researchers have also ventured into considering the structural similarity between the nitrides, M₂N (M = Ca, Sr) and carbides, M'₂C (M' = Ti, V, Nb). The metallic and layered characteristics make the monolayer M₂N suitable as electrodes for rechargeable batteries.^[20,21] Although transition metal sulphides, carbides and nitrides have been investigated, it is also fascinating to probe the efficacy of transition metal borides (TMBs) and their derivatives as anode material. Though theoretical studies^[22,23] identify titanium borides as potential anode candidates, there are no experimental shreds of evidence to date. Amorphous Co–B prepared by direct reduction method from CoCl₂, when used as an active material for LIB anode, exhibited a discharge capacity of 350 mAh g⁻¹ during its second discharge at 50 mA g⁻¹ current density.^[24] Since the Co–B as such exhibited a very drastic capacity fade, the electrochemical performance of its composite with rGO was investigated in the paper. In general, metal borides are hard and inert; however,

[a] Dr. S. Suriyakumar, V. Surendran, Dr. M. M. Shajumon
School of Physics

Indian Institute of Science Education and Research Thiruvananthapuram
Maruthamala PO, Vithura, Thiruvananthapuram, Kerala 695551, India
E-mail: shajju@iisertvm.ac.in

[b] A. Varma, Dr. K. Jasuja
Faculty of Chemical Engineering
Indian Institute of Technology Gandhinagar
Palaj, Gujarat 382355, India
E-mail: Kabeer@iitgn.ac.in

 Supporting information for this article is available on the WWW under
<https://doi.org/10.1002/batt.202100243>

recent studies reveal that the exfoliation method could easily enable the dissolution of these borides in water or dilute aqueous solutions of H_2O_2 and further self-assemble to form boron-rich nanosheets. Interestingly, another work emphasises the merits of a similar experimental approach.^[25] In their work, V_2O_5 nanobelts are applied as the cathodes in LIB and SIB, delivering 144 mAh g^{-1} at 20°C in LIBs and 61 mAh g^{-1} at 10°C in SIBs, respectively.

We, for the first time, report the use of nanosheets derived from TiB_2 as anode materials of SIBs. Though exfoliation is the widely adopted strategy towards preparing nanosheets, the procedure offers less yield and is difficult to control the thickness. Further, the non-uniformity and small domain size of mechanically exfoliated 2D materials is a long-term problem. Alternative approaches, including chemical vapour deposition, molecular beam epitaxy, and atomic layer deposition, have also been employed, each of which has its own merits and demerits. A recent work reports the preparation of amorphous Co–Ni–B–O nanosheets by the chemical reduction of a Co–Ni Prussian blue analogue precursor using sodium borohydride for the first time.^[26] In an unconventional approach, we provide a novel and scalable non-classical recrystallization procedure for the synthesis of TiB_2 -derived nanosheets with high-yield.^[27] Such dissolution recrystallization-based synthesis methodology is scarcely reported for battery application and that it holds potential for scaling up towards large-scale industry applications.

2. Results and Discussion

2.1. Physico-Chemical Characterization

Fluffy pale yellow coloured titanium diboride-derived nanosheets (TiB_2 -NS) are prepared by subjecting bulk TiB_2 powder to react with H_2O_2 . The schematic representation of the synthesis procedure is depicted in Figure S1(a). Given that H_2O_2 is commonly used as an active component for synthesizing graphene nanosheets via the exfoliation of graphite by spontaneous intercalation process, we expected a similar exfoliation mechanism.

Figure 1(a) shows the SEM image of the TiB_2 sheet-like structures. Since the TiB_2 -NS are larger than the precursor TiB_2 powder, it is assumed that the TiB_2 undergoes initial dissolution followed by prenucleation of clusters to assemble as nanosheets through non-classical recrystallization.^[27] This process introduces additional oxygen functional groups, as evidenced in EDX spectra (Inset Figure 1a). The silica substrate accounts for the large Si peak and a fraction of the oxygen peak. Figure 1(b) shows the AFM topography of a nanosheet and the corresponding 2D height profile of the TiB_2 -NS. The nanosheets have large lateral dimensions, and the height profile reveals that the TiB_2 -NS are $\sim 20 \text{ nm}$ thick. Figure 1(c,d) shows the HRTEM image of the nanosheets at different magnifications. The presence of layered morphology is evident in Figure 1(d). Further, the inset in Figure 1(d) shows bright spots forming two rings in the SAED pattern, indicating polycrystalline nature. The

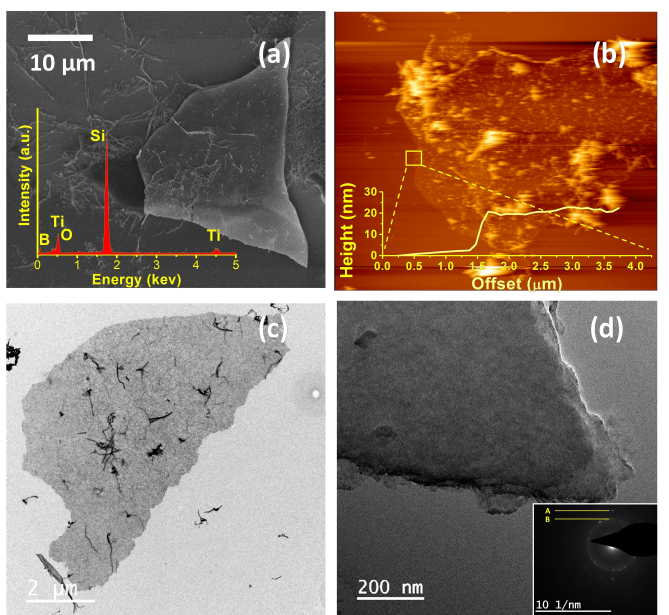


Figure 1. a) SEM image of the TiB_2 -derived nanosheets. (Inset: EDX spectrum). b) Atomic force micrograph of the TiB_2 -NS and the height profile showing the thickness of the nanosheet section marked in a square. c) Low and d) high magnification TEM image of the TiB_2 -NS. Inset of d) shows SAED pattern obtained from the edge of the nanosheet.

interlayer spacing will be discussed in detail in the later section. The XRD studies of TiB_2 -NS (Figure S1b) reveals that the nanosheets exhibit modified pattern, unlike their parent TiB_2 bulk powder (Figure S1d and e). This change in the crystal structure may be ascribed to the chemical modification during synthesis. A more detailed characterization of the physicochemical and rheological properties of the as-prepared nanosheets and a more in-depth insight into the formation mechanism is presented elsewhere.^[27]

2.2. Electrochemical Studies: TiB_2 -NS vs. Sodium Metal Half-Cell

To investigate the electrochemical behaviour of TiB_2 -NS, a cyclic voltammogram (CV) of electrode comprised of TiB_2 -NS vs. sodium metal scanned between 0.01 and 2.5 V is carried out at 0.1 mV s^{-1} at 20°C , and the first three cycles are provided in Figure 2(a). The initial large reduction peak is attributed to the first sodiation process. The significant sodium ion uptake and the likely formation of Na_xTiB_2 occur between 0.6–0.2 V vs. Na/Na⁺, while the desodiation mainly occurs below 1 V vs. Na/Na⁺. The initial sharp hump during the oxidation scan in the first cycle is characteristic of the Super P carbon present in the sample.^[28] The peak disappears in the subsequent cycles, indicative of Super P's negligible contribution to the cell capacity.

The electrode composition was varied and the optimal ratio was chosen based on the electrochemical performance (Table S1). Anode 1 (the better performing cathode of all the four compositions) comprises 50% TiB_2 -NS, 40% Super P, and 10%

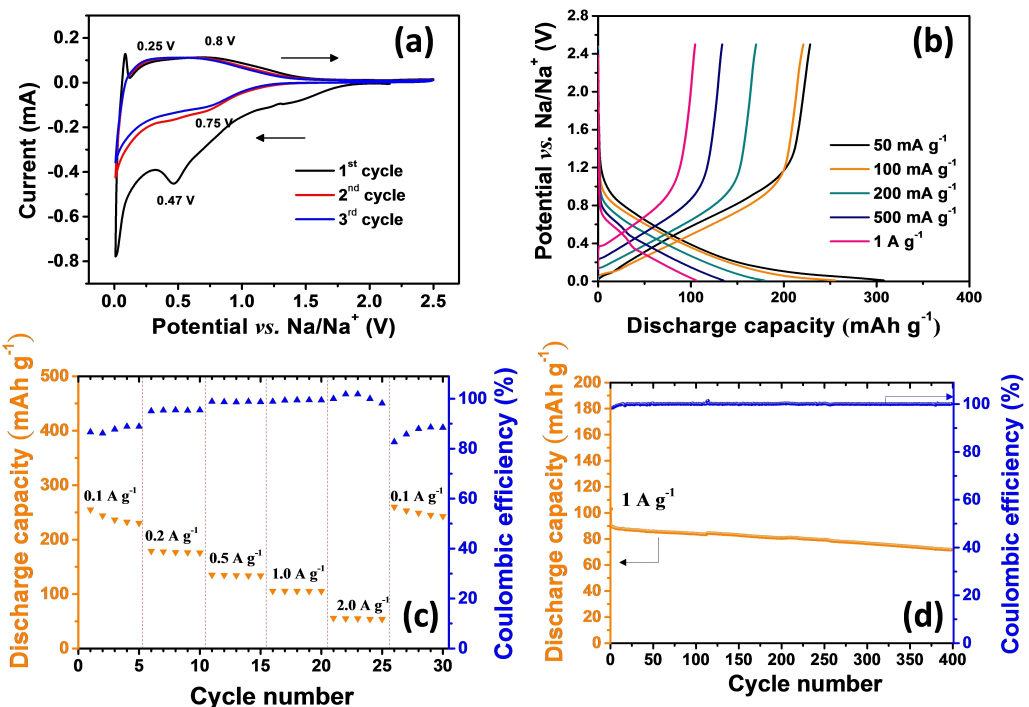


Figure 2. a) Cyclic voltammogram of TB-NS electrode at a scan rate of 0.1 mVs^{-1} for the initial three cycles, b) Galvanostatic cycling profile, c) rate capability at different current rates and d) capacity retention plot of TB-NS half cells cycled at 1 Ag^{-1} for 400 cycles.

PVdF binder. The cycling profile of the half cell at various current density is depicted in Figure 2(b). The cell delivers an initial discharge capacity of 304 and 252 mAh g^{-1} , respectively, at 50 and 100 mA g^{-1} . The rate capability studies plotted in Figure 2(c) reveal that the cell delivers a discharge capacity of 185, 136, 103, and 55 mAh g^{-1} at 0.2 , 0.5 , 1 , and 2 Ag^{-1} . It should be mentioned that the cell can discharge 255 mAh g^{-1} when cycled back at 0.1 Ag^{-1} , indicating good structural stability of the electrode. The cycling stability of the anode is tested at 1 Ag^{-1} . The specific discharge capacity at the 1st and 400th cycle was 89 and 71 mAh g^{-1} , respectively. It is also very promising to note that the capacity fade per cycle is $0.0045 \text{ mAh g}^{-1}$. The Coulombic efficiency was correspondingly averaged to 99.9% (Figure 2d). Figure S2 shows the SEM image of the electrode before and after cycling. As depicted in Figure S2(b), the nanosheets are homogeneously dispersed, and have not undergone any structural wear and tear post cycling. However, a few solid depositions are observed on the surface of the nanosheets, which may be attributed to the species formed during sodiation. Upon replacing 20% of Super P with graphite (Anode 2), we found a significant drop in discharge capacity. As seen in Figure S3(a), Anode 2 delivered a discharge capacity of 124 mAh g^{-1} at 0.1 Ag^{-1} . Though graphite is an excellent electronic conductor, it is a poor candidate for sodium intercalation and would possibly block the ion conduction pathway in the electrode. The increase in TiB_2 concentration from 50% to 60% in Anode 3 also contributed to a significant reduction in the specific discharge capacity (Figure S3b). Table S2 summarizes the first discharge capacity at various current densities. As seen from the table, the cell delivered a

much-reduced capacity of 108 mAh g^{-1} at 0.1 Ag^{-1} . The decrease in discharge capacity could be attributed to the poor conductivity of $\text{TiB}_2\text{-NS}$.

Notwithstanding that Super P carbon can also contribute to the electrode's net capacity, we fabricated an electrode composed of 90% Super P and 10% binder (Anode 4). The cycling profile and rate capability of the half-cell constituting Anode 4 are presented in Figure S3(c). At 0.1 and 1 Ag^{-1} current density, the cell delivers 105 and 48 mAh g^{-1} , respectively. Only 64 mAh g^{-1} is achieved when the cell is cycled back at 0.1 Ag^{-1} . This could be because of the poor kinetics of Super P upon cycling at high currents.^[19] 40% Super P is incorporated in the better performing anode composition. Simple calculations show that the Super P could have contributed to a maximum of 86 mAh g^{-1} towards the net 252 mAh g^{-1} of the better performing anode composition (Anode 1, labelled as "TB-NS" henceforth) at 0.1 Ag^{-1} . Further, Super P carbon-based anodes exhibit a characteristic charging profile with a hump in the lower potential, as seen from the inset in Figure S4. This hump is not explicit in the other compositions indicating the negligible contribution of Super P. At this juncture, it is also vital to emphasize that this unique method of recrystallization has introduced sites for charge storage. Bulk TiB_2 , from which the nanosheet was derived, was used as active material in the same composition ratio, which was found optimum for the nanosheets. It is observed from Figure S5 that the discharge capacity of the anode is similar to that of the bare-Super P anode (Figure S4), which reflects upon the strangeness of bulk TiB_2 towards sodium storage. From these results, it is evident that the chemically modified

TiB₂-derived nanosheets can efficiently host sodium ions and is a promising anode material.

The sodium ion kinetic parameters in the TB-NS anode are studied through GITT measurements.^[29] The host TB-NS electrode is sodiated/de-sodiated with a current density of 35 mA g⁻¹ for 10 min, which causes a change in the chemical potential. The sodium ion diffusion coefficient (D_{chem}) and the partial Na⁺ conductivity is determined by solving Fick's second law of diffusion through a series of assumptions and simplifications (See Section 1.1 of Supporting Information). Figure 3(a) represents the GITT curve of TB-NS during the 5th cycle. The inset depicts the GITT steps at a small time interval. A single GITT step with input parameters such as τ , relaxation time, iR drop, ΔE_t and ΔE_s clearly labelled is presented in Figure 3(b). Similar to hard carbon anodes,^[30] the initial slope region during discharge is associated with the adsorption capacity, the relatively flat region less than 0.4 V vs. Na/Na⁺ is associated with the intercalation capacity. Accordingly, this intercalation mechanism is reflected in the D_{chem} vs. potential plot shown in Figure 3(c) as a drop in D_{chem} for potential less than 0.4 V vs. Na/Na⁺. In the charging region, a drop in D_{chem} is observed around 0.9 V vs. Na/Na⁺, which is the region of the transition of the capacity contribution from intercalation mechanism to absorption mechanism. The D_{chem} value is in the order of 10⁻¹⁰, which can be attributed to the large lateral dimensions of the nanosheets. A minimum chemical diffusion coefficient at ~1.0 V during discharging and charging indicates the partial phase transformation point, where more energy is needed for the insertion or removal of Na-ions inside the lattice.^[29] A similar work on TiS₂ grown by atomic layer deposition over stainless steel spacer disk shows that the Na⁺ intercalation in

TiS₂ (with NaClO₄ in EC: DMC electrolyte) yielded a diffusion coefficient (D_{Na^+}) in the range of 7.30×10^{-17} to 3.93×10^{-13} cm² s⁻¹ in the voltage range from 1.91 to 0.56 V, through GITT studies. In another work, electrode prepared with doped porous hollow carbon confined SnS nanospheres particles and Super P carbon exhibited diffusion coefficient (D_{Na^+}) in the same order of TB-NS electrode.^[31] This enhanced value may be attributed to the significant contribution of Super P towards achieving good electrical contact and wettability between the current collector and electrolyte with the nanosheets, respectively.

The partial sodium ion conductivity (σ_{Na^+}) at various potentials during discharge and charge is shown in Figure 3(d). It is fascinating to observe the trend of the plot as we notice a hike in σ_{Na^+} values at the potentials corresponding to the intercalation/de-intercalation domains in the charge-discharge. The reduced σ_{Na^+} values at the beginning of discharge and end of charge are ascribed to the diffusion limitations offered by the nanosheets.

Having established the sodium ion intercalation mechanism, we further performed the CV of the TB-NS vs. Na at various scan rates (Figure 4a), ranging from 0.1–5 mV s⁻¹, to understand the kinetics of sodium ions in TB-NS.^[29] The anodic b -value is obtained from the slope of $\log(i_p)$ vs. $\log(v)$ plot shown in Figure 4(b). The value of b determines two well-defined conditions: for $b=0.5$, the current is controlled by semi-infinite linear diffusion, which could indicate a faradaic intercalation process, and $b=1$ is attributed to a surface controlled capacitive response.^[32] The reduction in b -value to ~0.65 in the region higher than 1 mV s⁻¹ is indicative of a diffusion-limited reaction process.

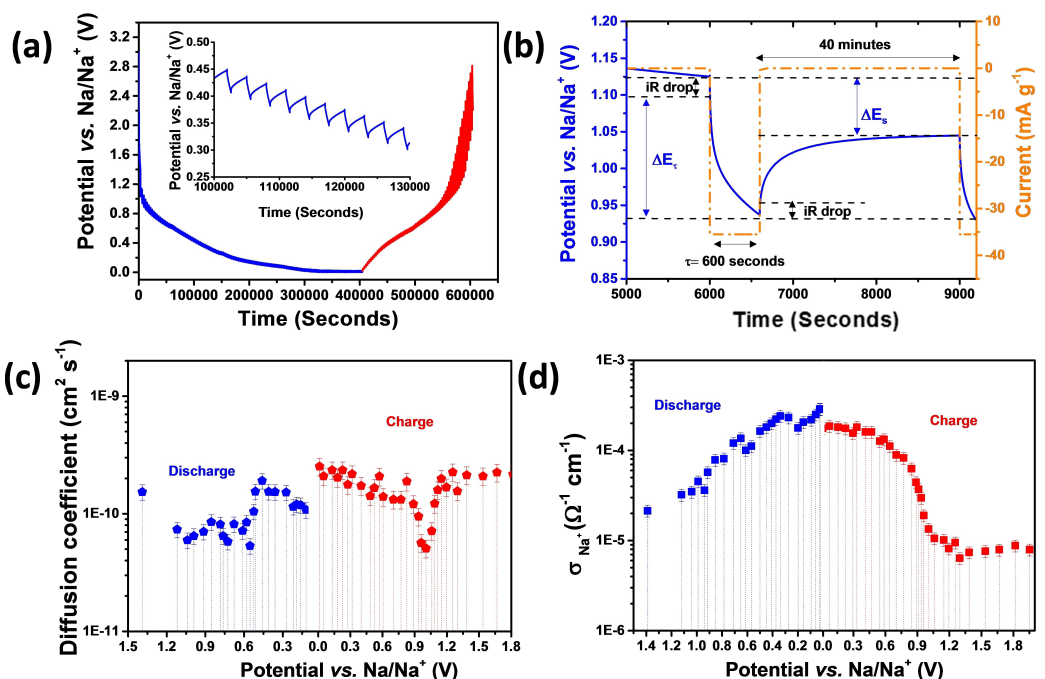


Figure 3. a) GITT curves of TB-NS during the 5th cycle. Inset: zoomed view of GITT steps, b) single-step GITT profile recorded between $t = 6000$ to 9000 seconds, c) chemical diffusion coefficient and d) partial conductivity of sodium ions during charge and discharge.

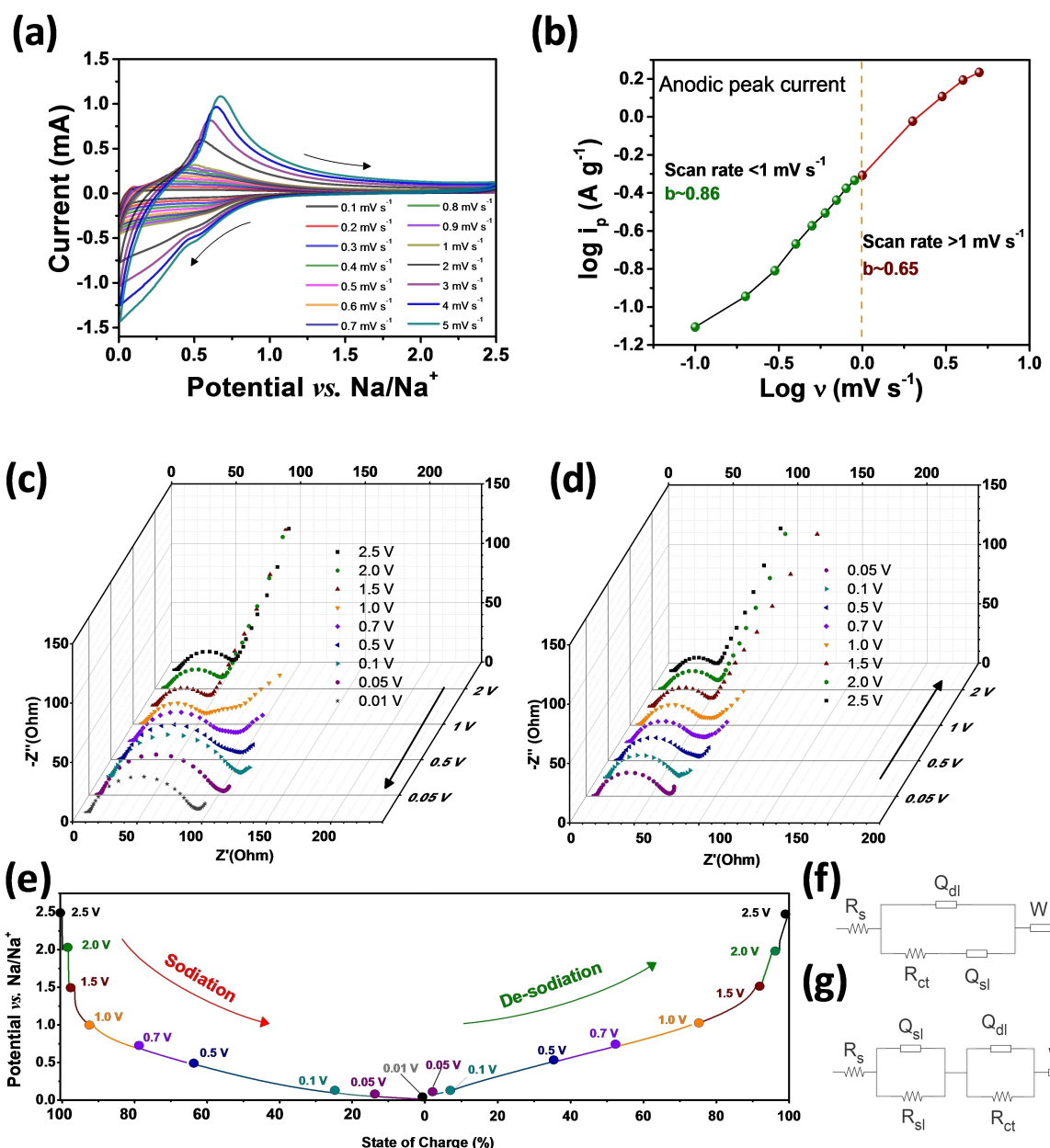


Figure 4. a) Cyclic voltammogram of TB-NS anode at different scan rates, b) plot showing specific peak current (i_p) vs. sweep rates (v) ranging from 0.1 to 5 mV s⁻¹. EIS measurements during c) sodiation and d) desodiation at the intermittent state of charge. e) Discharge-charge profile indicating various potentials at which EIS measurements were carried out. f) and g) Equivalent circuits used to fit the Nyquist plots.

Electrochemical impedance spectroscopy is a powerful tool to probe the dynamics of charge carriers.^[33–35] The study of the evolution of Nyquist plot at various depth of discharge and state of charge is a very versatile approach to understand the behaviour of a given anode by applying a small excitation voltage to the working electrode (TB-NS in our case) and recording the resulting response.^[36] Excitations at multiple frequencies and various SOCs allow the investigation of several electrochemical transport phenomena occurring at different time scales which facilitates the development of equivalent circuit models for performance estimation. Figure 4(c and d) shows the Nyquist plots measured at various potentials during sodiation and de-sodiation, respectively. For better understand-

ing, a single charge-discharge cycle marking the potential and SOC at which EIS measurements were carried out is presented in Figure 4(e). It is found from the shape of the Nyquist plot that there is a change in cell dynamics during charge-discharge. In particular, we notice the appearance of an additional semicircle in the potential between 1.0 and 0.5 V (during sodiation and de-sodiation), which is due to the change in the sodium ion intercalation and de-intercalation mechanism. Therefore, it is acknowledged that two equivalent circuit models, shown in Figure 4(f and g), provide a reasonable description of cell dynamics during a charge/discharge cycle at their respective potentials. The experimentally obtained plot is fit using EC lab software, and the value of the corresponding

components is presented in Table S3. R_s represents the solution resistance in both the equivalent circuits, which depends on the connectivity of wire, electrolyte concentration, etc. No much change in R_s value is observed (~ 8 Ohm), indicative of a typical ion intercalation process. It also corroborates the absence of dissolution of species inside the electrolyte. Further, R_{ct} in parallel combination with Q_{dl} contributes to a semicircle congruent to the charge transfer process at the electrode-electrolyte interface. A significant increase in charge transfer resistance observed upon sodiation can be ascribed to the increase in the accumulation of Na^+ ions in the nanosheets. The Warburg impedance associated with the diffusion of charged species is indicated by a line in the low-frequency region.^[37] As mentioned earlier, the appearance of two semicircles is noted in the intermediate potential. A similar observation was noted in the Nyquist plot of anode comprised of exfoliated MoS_2 nanosheets and rGO.^[38] The semicircle in the high-frequency region is attributed to the surface passivation layer, and the one in the medium frequency (MF) is mapped to the charge transfer at the electrode/electrolyte interface. The CPE denoted as Q_{sl} has α close to 1, which indicates a purely capacitive behaviour. During the entire sodiation process, it is found that the value of Q_{sl} increases with sodiation from 5.86×10^{-3} to $1.20 \times 10^{-1} \text{ F s}^{(\alpha-1)}$ (Table S3). This increase in Q_{sl} could be because of the intercalation of sodium ions into the nanosheets, causing exfoliation and exposure of fresh sites for SEI formation. A slight decrease in double-layer capacitance is also observed during the process. On the other hand, the value of R_{ct} increases from 40 to 78 Ohm, a steady increase is observed. In the subsequent desodiation process, similar to sodiation, two distinct EIS profiles are obtained. The value of R_{ct}

and Q_{dl} associated with the faradaic process and solution resistance remains almost constant. The large lateral surface of the nanosheets as evidenced from the SEM image, contribute to a short ion diffusion path which could possibly be the reason for no explicit variation in charge transfer resistance. Contrary to the sodiation process, we also find a decrease in Q_{sl} value attributed to the de-intercalation and dissolution of ions from the periphery of the nanosheets into the electrolyte. Though we propose intercalation mechanism, an in-depth study is required to understand the Na-ion storage mechanism in detail. To probe the intercalation of sodium ions in TB-NS, TEM and XPS analyses have been carried out and presented in the following section.

2.3. Post Cycling Analysis

Various in-situ and ex-situ spectroscopic techniques such as Raman, EDS and XPS studies are commonly used to understand the structural and compositional changes in the battery electrode upon cycling.^[39-41] Since the TB-NS were very light and fluffy, the Raman signals were feeble. To overcome the issue, 25 mg of powder was gently pelletized by applying a pressure of fewer than 2 Tons. Raman studies performed on the TB-NS pellets before and after sodiation (Figure S6a) showed additional sharp Raman peaks at 718 and 902 cm^{-1} , which could be attributed to sodium complexes. To unveil the underlying reaction mechanism, the high-resolution Titanium XPS spectrum of TiB_2 -derived nanosheet, and sodiated and de-sodiated TiB_2 electrode is obtained and is presented in Figure 5(a). Ti 2p has a significant split in spin-orbit components

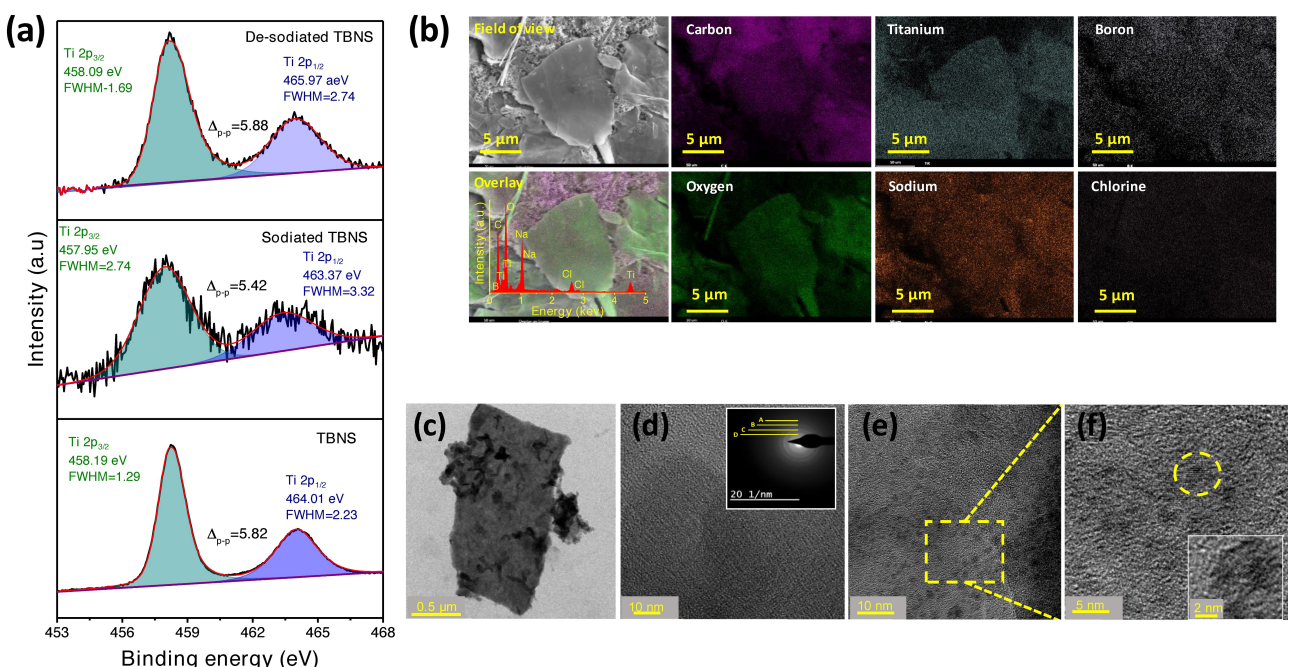


Figure 5. a) High-resolution Ti 2p XPS spectra of pristine, sodiated and de-sodiated TB-NS anode. b) SEM elemental mapping and c) TEM image of sodiated TiB_2 electrode. d) HR-TEM image of the TB-NS and its SAED (Inset). e) HR-TEM image at another region of the sodiated anode and f) its zoomed image and the region of localised lattice fringes.

to $\text{Ti}2\text{p}_{3/2}$ at 458.2 eV and $\text{Ti}2\text{p}_{1/2}$ at 464.0 eV. The sodiation process is responsible for the shift in binding energy values of the $\text{Ti}2\text{p}_{3/2}$ from 458.2 to 457.9 eV and $\text{Ti}2\text{p}_{1/2}$ from 464.0 to 463.3 eV during sodiation process. It is worth mentioning that these effects are predominantly reversible because the peak shifts due to sodiation are reversed after de-sodiation, and the peak intensities are restored. We also observe the broadening of the peaks upon sodiation and a reversal upon de-sodiation. In general, the broadening of a peak may indicate a change in the number of chemical bonds contributing to a peak shape, a change in the sample condition and differential charging of the surface (localized differences in the charge state of the surface).

The interpretation of ion intercalation through XPS was a challenging task, owing to the following factors: a) In addition to the poor sensitivity of boron 1s peak, the presence of NaClO_4 in the electrolyte contributed to a very high intense $\text{Cl}2\text{p}$ peak. This shadows the B 1s region of the TiB_2 sample in the sodiated and de-sodiated state, b) the presence of Na KLL Auger emission at ~ 535 eV masks the O 1s region of the spectrum. c) The Na 1s peak is strongly overlapped by Ti LMM Auger peaks. Though challenging, we can substantiate the intercalation using $\text{Ti}2\text{p}$ spectra. Further, as an additional parameter, the atomic weight percentage ratio of sodium to titanium was calculated from the survey spectra (Figure S6b) for the sodiated and de-sodiated state, which is a quasi-quantificational method to estimate sodiation in the electrode.^[42] From Figure S6(c), the ratio of Na/Ti is high in the survey spectrum of the sodiated electrode than the de-sodiated electrode, which indicates that sodium is accommodated in the electrode. The elemental mapping of sodiated TiB_2 in Figure 5(b) also show considerable coverage of Na species over the TB-NS flakes.

To further probe the microstructural transformation and ion diffusion of the anode directly at the atomic scale during sodiation and desodiation processes, TEM and HRTEM analysis of a cycled TB-NS anode is obtained in its sodiated state and presented in Figure 5(c) along with the SAED pattern (Figure 5d). On comparing the sodiated TiB_2 sheets with the TB-NS scraped from a pristine electrode and bare TiB_2 sheets (Figures S7–S9), surface passivation is observed on top of the sheets. It is also interesting to observe regions with percolation pathways indicative of ion migration. We observe from the SAED pattern in Figure 5(d) that the anode's crystallinity has been altered due to repeated ion intercalation and extraction. The interlayer spacing estimated from the SAED pattern shows an increase from ~ 2.9 to ~ 3.5 Å (Figure S10). We anticipate that the breathing of the TiB_2 lattice during ion intercalation could have resulted in the expansion. Similar observations are reported for PTCDA-derived soft carbon, wherein expansion from ~ 3.6 to 4.2 Å was noted.^[43] Even a greater extent of expansion from 6.3 to 9.8 Å was reported in MoS_2 sheets.^[38] On the contrary, a work on MXene as anode material validates that the interlayer distance is maintained during the whole sodiation/desodiation process.^[44] The authors attribute this effect to the pillarizing effect of trapped Na^+ and the swelling effect of penetrated solvent molecules between the $\text{Ti}_3\text{C}_2\text{T}_x$ sheets. Interestingly, the intermittent regions with circular

patches (Figure 5e and f) show lattice fringes near the surface similar to that of hard carbon anodes reported elsewhere.^[45]

2.4. Full-Cell Studies

The appreciable performance of TB-NS as an anode encouraged us to study the full cell performance by assembling a prototype coin cell with $\text{Na}_3\text{V}_2(\text{PO}_4)_3/\text{C}$ (NVP-C) and TB-NS as cathode and anode, respectively. After characterizing the NVP-C using XRD (Figure S11), it was employed as the cathode active material in a full cell. The electrode was initially tested in half-cell configuration with sodium as a counter/reference electrode. It was found that the half-cell delivered an initial capacity of 108 and 90 mAh g^{-1} at 0.1 and 1C-rate (theoretical capacity = 117 mAh g^{-1}) (Figure S12). Before full cell assembly, the TB-NS anode is sodiated at 100 mA g^{-1} current density. The cell is assembled in a 1.2:1 active mass ratio and is first activated by charging to form the sodium intercalated anode and de-intercalated cathode in the fully charged cell. The CV curves of the full cell recorded at various scan rates are shown in Figure S13. The CV curve shows a prominent reduction peak, 2.79 V and oxidation peak, 2.84 V, which corresponds to the range that controls the battery's operational potential. The voltage window of the cell is fixed from 1.0 to 4.0 V and cycled at various current densities. The specific capacities are evaluated based on the total mass loading of the active materials. The TB-NS/NVP-C cell delivers discharge capacity of 48, 35, 27 mAh g^{-1} at 0.2, 0.5 and 1 A g^{-1} , respectively, and can discharge 31 mAh g^{-1} when cycled back at 0.5 A g^{-1} current density (Figures 6a,b and S14). These results suggest that the electrodes preserve structural integrity even after cycling at high current densities.

Further optimization of the full cell performance, taking into account the rate capability and capacity, is required. To understand the device properties, the energy density and power densities were calculated^[46] and are represented in the Ragone plot shown in Figure 6(c). A high energy density of 111 Wh kg^{-1} is obtained at a power density of 0.5 kW kg^{-1} , and the device shows an energy density of $\sim 20 \text{ Wh kg}^{-1}$ even at 8 kW kg^{-1} . Moving one more step closer to a real-time application, 58 LEDs arranged to read "IISER TVM" was designed as shown in Figure S15 and lighted using the fabricated full cell (Inset of Figure 6). Altogether, this study explores the potential offered by the TiB_2 -derived nanosheets in energy storage applications.

3. Conclusions

In summary, the present study investigates the sodiation/desodiation behaviour of TiB_2 -derived nanosheets for potential application in energy storage. The work reported here forms the maiden effort in exploring the experimental viability of boride-based material as anode for Na-ion battery. Nonetheless, this work upholds the recent theoretical reports highlighting the suitability of boride materials, as an anode in a sodium-ion

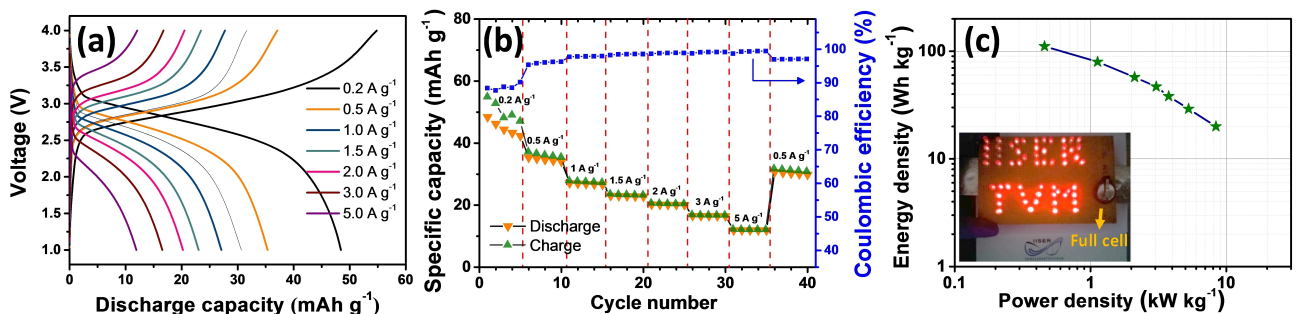


Figure 6. Electrochemical performance of the TB-NS//NVP-C full cell prototype cycled in the potential window of 1 to 4 V. a) Cycling profile and b) rate performance of the TB-NS//NVP-C full cell at various current rates. c) Ragone plot for the full cell. Inset: Practical demonstration of the full cell prototype, showing the lighting of LED lights powered by a coin cell.

battery. Prepared through a scalable dissolution-recrystallization approach, the nanosheets when explored as anode material deliver an initial discharge capacity of 252 mAh g^{-1} at 0.1 A g^{-1} , and appreciable cycling stability is achieved at 1 A g^{-1} current density. Using ex-situ HRTEM and XPS analyses along with electrochemical studies viz, GITT and EIS, the mechanism of Na-ion storage in the nanosheets was investigated. Further, the fabricated full-cell prototype showed good overall electrochemical behaviour. These results potentially encourage the use of borides as an anode for sodium-ion batteries. Further optimization in terms of structure engineering and incorporation of electrolyte additives as a stabilizer may be the direction of future research.

Experimental Section

Synthesis of chemically modified TiB_2 nanosheets

TiB_2 derived nanosheets ($\text{TiB}_2\text{-NS}$) have been prepared through a one-pot chemical route, pioneered by Jasuja et al.^[27] Briefly, 300 mg of TiB_2 powder with particle size $< 10 \mu\text{m}$ procured from Sigma Aldrich, 99.5% pure, was added to 90 mL of deionized (DI) water and gently stirred at 250 rpm for 10 min to obtain a black colour suspension. 10 mL of aqueous H_2O_2 (Merck, 30%) was added to the suspension drop by drop, and the resultant mixture was stirred for one hour at room temperature. A change in colour from black to murky yellow was observed within a few minutes of mixing. Subsequently, the mixture, which turned completely yellow, was kept undisturbed for 24 hours. Black solid sediment was observed at the bottom phase, leaving a yellow phase at the top, which was collected and subjected to centrifugation at 8000 rpm for 30 min at 20°C to pellet out any heavier particles. A purified aqueous dispersion containing nanosheets was obtained upon subjecting the supernatant to dialysis (Thermo Fisher, Snake-skin dialysis tubing, molecular weight cut-off of 10 kDa) against DI water for 24 h. To obtain nanosheets in a powder form, the purified aqueous dispersion was kept for freeze-drying at -4°C for 24 h, after which it was subjected to lyophilisation (Martin Christ Alpha-2D Plus) for 48 to 72 h. Lyophilizing 10 mL of the dispersion resulted in ~ 30 mg of pale yellow coloured fluffy powder.

Preparation of $\text{Na}_3\text{V}_2(\text{PO}_4)_3$ -carbon composite (NVP-C)

$\text{Na}_3\text{V}_2(\text{PO}_4)_3$ powder was prepared as reported elsewhere.^[47] Briefly, NaOH , NH_4VO_3 , $\text{NH}_4\text{H}_2\text{PO}_4$ were mixed in the molar ratio of 3:2:3

(Na:V:P) in 25 mL of deionized water. $\frac{1}{3}$ mol of citric acid (3.2 g) was added to the solution and kept for stirring at 80°C for 8 h. The resultant, a dark blue gel, was dried at 80°C for 12 h in an air oven. The product thus formed was crushed and calcined at 350°C for 3 h. This was followed by calcination at 800°C for 16 h in under argon atmosphere. The proper calcination temperature can ensure high crystallinity and good crystal structure of the prepared samples. The final product was made into a fine powder using a mortar and sieved using a 25 μm sized mesh to obtain particles of size not exceeding 25 μm . XRD studies were carried out to confirm the formation of $\text{Na}_3\text{V}_2(\text{PO}_4)_3$.

Materials characterization

SEM imaging and EDS analysis were performed with a scanning electron microscope (SEM; Nova NanoSEM 450, FEI). The thickness of the nanosheets was analysed using an atomic force microscope (AFM). Samples dispersed in iso-propanol were drop-casted onto silicon substrate for SEM and AFM imaging. Prior to SEM imaging, the samples were sputtered with gold to improve surface conductivity. High-resolution transmission electron microscope (HRTEM) imaging and selected area electron diffraction (SAED) studies were carried out using FEI TECNAL 30 G2 S-TWIN microscope with an accelerating voltage of 300 kV. A minimal amount of sample was added to Iso-propanol and sonicated for 10 min to obtain a uniform dispersion. The dispersion was then carefully drop casted onto Cu grids of 400 mesh size for HRTEM imaging. Powder XRD measurements were carried out with $\text{Cu}-\text{K}_{\alpha}$ radiation within Bragg's angle ranging from 10° to 80° (Empyrean, PANalytical XRD system). High-resolution X-ray photoelectron spectroscopy (XPS) was carried out using an ESCA Plus spectrometer (Omicron Nanotechnology Ltd, Germany, using $\text{Mg}-\text{K}\alpha$ source). CASA XPS software was used for the deconvolution of peaks. The Raman spectra were collected from a Raman spectrophotometer (Horiba Xplora) with a 638 nm laser source.

Electrochemical studies of half-cell

TiB_2 -derived nanosheets ($\text{TiB}_2\text{-NS}$) were used as the active material for electrode preparation. Briefly, 50% $\text{TiB}_2\text{-NS}$, 40% Super P conducting carbon, and 10% polyvinylidene fluoride (PVDF) binder were mixed in 400 μL of NMP solvent. The slurry was then coated onto a copper foil and dried at 100°C in a vacuum oven. 14 mm electrode discs having a thickness of $\sim 30 \mu\text{m}$ and active mass loading of 0.7–1.0 mg was cut from the coated foil for use as electrode. For comparison, electrodes were prepared with varying composition as detailed in Table S1. For electrochemical half-cell measurements vs. sodium metal, CR2032 coin cells were assembled

in a glove box filled with argon. The electrolyte was 140 μL of 1 M NaClO₄ in ethylene carbonate (EC) and dimethyl carbonate (DMC) (1:1 in volume). Glass microfiber membrane (Cat. No. 1823 090 WhatmanTM) was used as the separator. All Electrochemical measurements were done using a Bio-logic VMP3 workstation. Cyclic voltammetry (CV) was carried out in the voltage range from 0.01 to 2.5 V vs. Na/Na⁺. Galvanostatic measurements were made in the potential window at varying current densities. The specific capacities of the electrodes were evaluated based on the mass loading of TiB₂-NS. The better performing electrode composition is labelled "TB-NS" and is used for further electrochemical studies. Galvanostatic intermittent titration technique (GITT) was performed by applying current pulses (steps) for 10 min and subsequent relaxation for 40 min throughout one complete charge-discharge.^[29] Electrochemical impedance spectroscopy (EIS) measurements were carried out in a frequency range of 100 kHz to 100 mHz and an AC perturbation of 10 mV amplitude by varying the DC potentials.^[48] Similarly, the electrode composed of NVP-C, Super P and PVdF at a mass ratio of 75:15:10 was dried at 100 °C for 24 h under vacuum. Sodium metal foil was used as the anode, and the glass microfiber filter was used as the separator. The electrolyte was 140 μL of 1 M NaClO₄ in ethylene carbonate (EC) and dimethyl carbonate (DMC) (1:1 in volume). CV and galvanostatic charge-discharge measurements were carried out between 2.5 to 4.2 V vs. Na/Na⁺.

Fabrication and testing of TB-NS / NVP full-cell

To get a better insight into the efficacy of the anode, a full cell was fabricated using TiB₂-NS and NVP-C as anode and cathode, respectively. Prior to cell assembly, the TB-NS electrode was sodiated at 50 mAg⁻¹. The electrode's optimum mass ratio was found by evaluating the cell performance by varying the mass ratio of NVP-C: TB-NS to 3:1, 2:1 and 1.2:1. A thick slurry of NVP-C, Super P, and PVdF in 75:15:10 mass ratio was pasted onto stainless steel mesh (Alfa Aesar), dried at 100 °C in a vacuum oven and used as a cathode to ensure efficient mass balancing. The full-cell comprised of sodiated TB-NS (anode), the glass fibre separator activated in the electrolyte, and the NVP-C (cathode) in 2032-type coin cell configuration assembled in an argon-filled glove box (Mbraun, Germany), with oxygen and water levels at <0.1 ppm. 1 M NaClO₄ in 1:1 v/v ratio of EC:DMC was used as the electrolyte. Galvanostatic measurements were made in the voltage range from 1 to 4 V vs. Na/Na⁺ at varying current densities. The specific capacities of the full-cell were evaluated based on the total mass loading of TiB₂-NS and NVP-C.

Acknowledgements

The authors M.M.S, S.S and V.S thank IISER Thiruvananthapuram for access and utilization of characterization instruments. S.S gratefully acknowledges the financial support from the Science and Engineering Research Board, Department of Science & Technology, Govt. of India [File Number: PDF/2020/000209].

Conflict of Interest

The authors declare no conflict of interest.

Keywords: anode · dissolution-recrystallization approach · full-cell studies · nanosheets · sodium ion battery · titanium diboride

- [1] D. Larcher, J. M. Tarascon, *Nat. Chem.* **2015**, *7*, 19–29.
- [2] Z. Song, H. Zhou, *Energy Environ. Sci.* **2013**, *6*, 2280–2301.
- [3] D. Kundu, E. Talaie, V. Duffort, L. F. Nazar, *Angew. Chem. Int. Ed.* **2015**, *54*, 3432–3448.
- [4] W. Zhang, F. Zhang, F. Ming, H. N. Alshareef, *EnergyChem* **2019**, *1*, 100012.
- [5] V. Surendran, R. S. Arya, T. V. Vineesh, B. Babu, M. M. Shaijumon, *J. Energy Storage* **2021**, *35*, 102340.
- [6] Y. Jiang, X. Zhou, D. Li, X. Cheng, F. Liu, Y. Yu, *Adv. Energy Mater.* **2018**, *8*, 1800068.
- [7] K. Chayabukka, G. Mulder, D. L. Danilov, P. H. L. Notten, *Adv. Energy Mater.* **2018**, *8*, 1800079.
- [8] P. Ge, M. Fouletier, *Solid State Ionics* **1988**, *28*–*30*, 1172–1175.
- [9] Y. M. Chang, H. W. Lin, L. J. Li, H. Y. Chen, *Mater. Today* **2020**, *6*, 100054.
- [10] M. S. Whittingham, *Chem. Rev.* **2004**, *104*, 4271–4301.
- [11] Y. Liu, H. Wang, L. Cheng, N. Han, F. Zhao, P. Li, C. Jin, Y. Li, *Nano Energy* **2016**, *20*, 168–175.
- [12] D. Xu, H. Wang, R. Qiu, Q. Wang, Z. Mao, Y. Jiang, R. Wang, B. He, Y. Gong, D. Li, X. Hu, *Energy Storage Mater.* **2020**, *28*, 91–100.
- [13] Z. Lu, N. Wang, Y. Zhang, P. Xue, M. Guo, B. Tang, X. Xu, W. Wang, Z. Bai, S. Dou, *ACS Appl. Energ. Mater.* **2018**, *1*, 6234–6241.
- [14] Y. Zhang, N. Wang, Z. Lu, P. Xue, Y. Liu, Y. Zhai, B. Tang, M. Guo, L. Qin, Z. Bai, *Electrochim. Acta* **2019**, *296*, 891–900.
- [15] M. Mortazavi, C. Wang, J. Deng, V. B. Shenoy, N. V. Medhekar, *J. Power Sources* **2014**, *268*, 279–286.
- [16] J. Come, M. Naguib, P. Rozier, M. W. Barsoum, Y. Gogotsi, P.-L. Taberna, M. Morcrette, P. Simon, *J. Electrochem. Soc.* **2012**, *159*, A1368–A1373.
- [17] S. Nyamdelger, T. Ochirkhuyag, D. Sangaa, D. Odkhuu, *Phys. Chem. Chem. Phys.* **2020**, *22*, 5807–5818.
- [18] Y.-M. Li, Y.-L. Guo, Z.-Y. Jiao, *Curr. Appl. Phys.* **2020**, *20*, 310–319.
- [19] J. Hu, B. Xu, C. Ouyang, Y. Zhang, S. A. Yang, *RSC Adv.* **2016**, *6*, 27467–27474.
- [20] A. Walsh, D. O. Scanlon, *J. Mater. Chem. C* **2013**, *1*, 3525–3528.
- [21] K. Lee, S. W. Kim, Y. Toda, S. Matsuishi, H. Hosono, *Nature* **2013**, *494*, 336–340.
- [22] T. Bo, P. F. Liu, J. Xu, J. Zhang, Y. Chen, O. Eriksson, F. Wang, B. T. Wang, *Phys. Chem. Chem. Phys.* **2018**, *20*, 22168–22178.
- [23] Z. Ma, F. Sun, M. Dou, Q. Yao, Y. Liu, F. Wu, *Phys. Lett. A* **2020**, *384*, 126282.
- [24] D. Wang, J. Zhou, J. Li, X. Jiang, Y. Wang, F. Gao, *Chem. Eng. J.* **2019**, *360*, 271–279.
- [25] X. Rui, Y. Tang, O. I. Malyi, A. Gusak, Y. Zhang, Z. Niu, H. T. Tan, C. Persson, X. Chen, Z. Chen, Q. Yan, *Nano Energy* **2016**, *22*, 583–593.
- [26] T. He, J. M. V. Nsanzimana, R. Qi, J. Y. Zhang, M. Miao, Y. Yan, K. Qi, H. Liu, B. Y. Xia, *J. Mater. Chem. A* **2018**, *6*, 23289–23294.
- [27] A. L. James, M. Lenka, N. Pandey, A. Ojha, A. Kumar, R. Saraswat, P. Thareja, V. Krishnan, K. Jasuja, *Nanoscale* **2020**, *12*, 17121–17131.
- [28] B. Peng, Y. Xu, X. Wang, X. Shi, F. M. Mulder, *Sci. China-Physics, Mech. Astron.* **2017**, *60*, 64611.
- [29] B. Babu, M. M. Shaijumon, *Electrochim. Acta* **2020**, *345*, 136208.
- [30] Y. Jin, S. Sun, M. Ou, Y. Liu, C. Fan, X. Sun, J. Peng, Y. Li, Y. Qiu, P. Wei, Z. Deng, Y. Xu, J. Han, Y. Huang, *ACS Appl. Energ. Mater.* **2018**, *1*, 2295–2305.
- [31] Y. Wang, Y. Zhang, J. Shi, A. Pan, F. Jiang, S. Liang, G. Cao, *J. Mater. Chem. A* **2018**, *6*, 18286–18292.
- [32] H. Lindström, S. Södergren, A. Solbrand, H. Rensmo, J. Hjelm, A. Hagfeldt, S. E. Lindquist, *J. Phys. Chem. B* **1997**, *101*, 7717–7722.
- [33] M. Li, *Renewable Sustainable Energy Rev.* **2017**, *100*, 44–52.
- [34] N. A. Cañas, K. Hirose, B. Pascucci, N. Wagner, K. A. Friedrich, R. Hiesgen, *Electrochim. Acta* **2013**, *97*, 42–51.
- [35] E. Karden, S. Buller, R. W. De Doncker, *J. Power Sources* **2000**, *85*, 72–78.
- [36] U. Westerhoff, K. Kurbach, F. Lienesch, M. Kurrat, *Energy Technol.* **2016**, *4*, 1620–1630.
- [37] G. Barbero, I. Lelidis, *Phys. Chem. Chem. Phys.* **2017**, *19*, 24934–24944.
- [38] T. S. Sahu, S. Mitra, *Sci. Rep.* **2015**, *5*, 1–13.
- [39] E. Flores, P. Novák, E. J. Berg, *Front. Energy Res.* **2018**, *6*, 82.
- [40] V. Shutthanandan, M. Nandasiri, J. Zheng, M. H. Engelhard, W. Xu, S. Thevuthasan, V. Murugesan, *J. Electron Spectrosc. Relat. Phenom.* **2019**, *231*, 2–10.

- [41] G. Hasegawa, K. Kanamori, K. Nakanishi, K. Hayashi, *Langmuir* **2019**, *35*, 12680–12688.
- [42] S. Song, M. Kotobuki, Y. Chen, S. Manzhos, C. Xu, N. Hu, L. Lu, *Sci. Rep.* **2017**, *7*, 373.
- [43] W. Luo, Z. Jian, Z. Xing, W. Wang, C. Bommier, M. M. Lerner, X. Ji, *ACS Cent. Sci.* **2015**, *1*, 516–522.
- [44] S. Kajiyama, L. Szabova, K. Sodeyama, H. Iinuma, R. Morita, K. Gotoh, Y. Tateyama, M. Okubo, A. Yamada, *ACS Nano* **2016**, *10*, 3334–3341.
- [45] J. Pan, Y. Sun, Y. Yan, L. Feng, Y. Zhang, A. Lin, F. Huang, J. Yang, *JACS* **2021**, *1*, 1208–1216.
- [46] B. Babu, M. M. Shaijumon, *J. Power Sources* **2017**, *353*, 85–94.
- [47] S. Luo, J. Li, S. Bao, Y. Liu, Z. Wang, *J. Electrochim. Soc.* **2018**, *165*, A1460–A1465.
- [48] S. Suriyakumar, N. Angulakshmi, A. M. M. Stephan, *Nano-Structures & Nano-Objects* **2017**, *11*, 46–55; *Nano-Objects* **2017**, *11*, 46–55.

Manuscript received: September 10, 2021
Revised manuscript received: October 25, 2021
Version of record online: December 1, 2021
